Journal of Volcanology and Geothermal Research 206 (2011) 96–105

Contents lists available at ScienceDirect

Journal of Volcanology and Geothermal Research

journal homepage: www.elsevier.com/locate/jvolgeores

Evidence for high fluid/melt content beneath Krakatau volcano (Indonesia) from local earthquake tomography

Kairly Jaxybulatov [a,b,*], Ivan Koulakov [a,b], Malte Ibs-von Seht [c], Klaus Klinge [c], Christian Reichert [c], Börje Dahren [d], Valentin R. Troll [d]

[a] Institute for Petroleum Geology and Geophysics, SB RAS, Novosibirsk, 630090, Russia
[b] Novosibirsk State University, 2, Pirogova str, 630090, Novosibirsk, Russia
[c] Federal Institute for Geosciences and Natural Resources (BGR), Stilleweg 2, 30655 Hannover, Germany
[d] Dept. of Earth Sciences, CEMPEG, Uppsala University, Uppsala, Sweden

ARTICLE INFO

Article history:
Received 28 September 2010
Accepted 23 June 2011
Available online 13 July 2011

Keywords:
Seismic tomography
Krakatau
Volcanism
Magma chamber

ABSTRACT

Within the KRAKMON project for multiparameter monitoring of Anak Krakatau volcano (Indonesia), a network of temporary stations was installed on the islands of the Krakatau complex as well as in the surrounding areas of the Sunda Strait, Sumatra and Java. The network was operated from June 2005 until January 2006. More than 700 local events were recorded during this experiment, and travel times from these events were used to perform a tomographic inversion for P and S velocities and for the Vp/Vs ratio. In this study, special attention was paid to the validation of the computed model based on different tests, such as inversion of independent data subsets and synthetic modeling. Although the network configuration and the distribution of the events are not favorable for high-quality tomographic imaging, we have obtained some important and robust features which give information about sources of volcanic activity in the Krakatau complex. The most interesting feature of this study is a zone of high Vp/Vs ratio beneath the Krakatau complex. At depths down to 4 km depth we observe anticorrelation of higher P- and lower S-velocities that leads to Vp/Vs ratio higher than 2. This is a probable indicator of the presence of partially molten and/or with high fluid content material with a composition corresponding to deeper layers. It is important that the anomaly of high Vp/Vs ratio beneath the Krakatau complex appears to be separated in two parts at a depth of 5–6 km. This fits to results of geobarometric analysis that presume the existence of several levels of magma chambers beneath Anak Krakatau.

1. Introduction

Krakatau volcano is one of the most dangerous volcanoes in the world and thus attracts vital interest from researchers of different disciplines. Geographically located in Indonesia, between Sumatra and Java, it is a part of the Sunda Arc (Fig. 1). Along this arc, the plate boundary between Eurasia and the Indian-Australian plate hosts around 100 active volcanoes [Simkin and Siebert, 1994, Hilton and Craig 1989]. In the area of Java and Sumatra, the northward subduction of the Indian oceanic plate under the Sunda block occurs at a rate of about 6.8–7.2 cm/yr [DeMets et al., 1990]. The age of the subducted plate in this segment of the Sunda Arc is about 80–100 Ma [Müller et al., 1997], one of the oldest values observed for the oceanic crust in the Indian Ocean.

The angle of subduction changes from near perpendicular (13°) in front of Java to oblique (55°) in front of Sumatra (Jarrard, 1986). The Sumatran rotation has resulted in extension, as reported in Harjono et al. (1991) and associated thinning of the crust to ~20 km in the Sunda Strait, as compared to 25–30 km in Sumatra and west Java (Nishimura and Harjono, 1992) (Fig. 1). The contemporary Krakatau volcanic complex consists of four islands; Rakata, Sertung, Panjang and Anak Krakatau (Fig. 1) and it is part of a NNW-SSE trending lineament of Quaternary volcanic edifices which lies approximately parallel to the Java trench. Sertung and Panjang islands are remnants of a caldera formed after an earlier explosive eruption, recorded in local Javanese folk stories of the Book of Kings, or 'Pararaton' (Judd, 1889; Nishimura et al., 1986; Camus et al., 1987) and describes heavy rains of stone in the year 338 Saka (416 AD). While there is no direct evidence for an eruption of this size at that time, it could be a mistaken date for another eruption described for 535 AD (Wohletz, 2000). In addition to this, there is also evidence for an even older large ignimbrite eruption

* Corresponding author. Tel.: +7 9628410307.
E-mail addresses: jaxybulatov@gmail.com (K. Jaxybulatov), KoulakovIY@ipgg.nsc.ru (I. Koulakov), m.ibs@bgr.de (M.I. Seht), borje.dahren@geo.uu.se (B. Dahren), valentin.troll@geo.uu.se (V.R. Troll).

0377-0273/$ – see front matter © 2011 Published by Elsevier B.V.
doi:10.1016/j.jvolgeores.2011.06.009

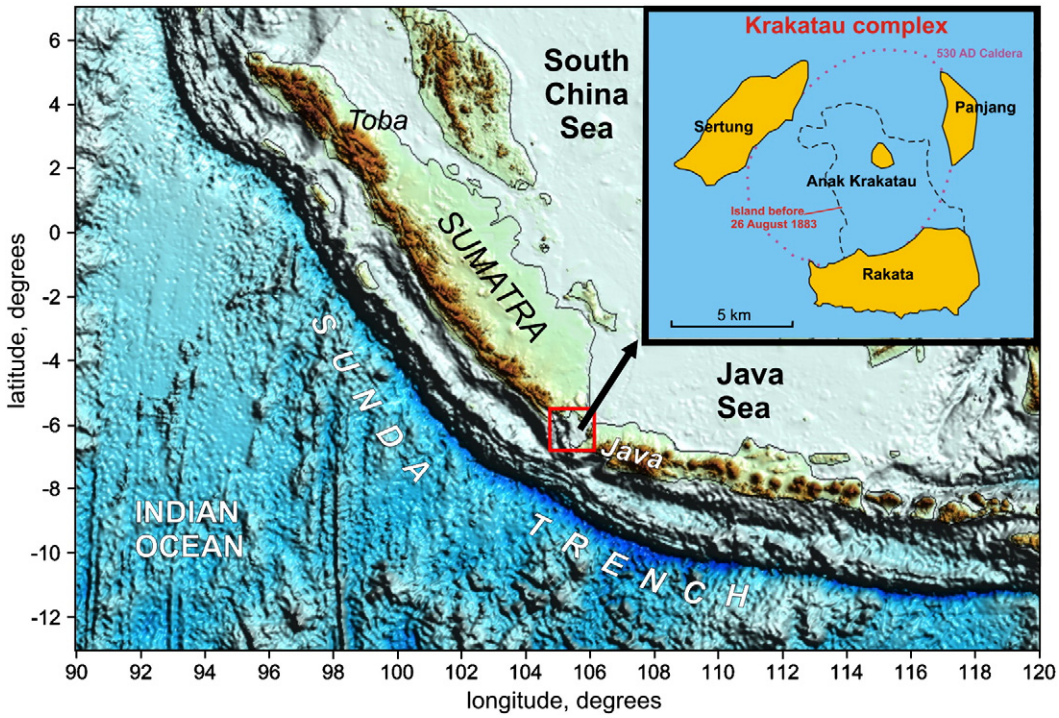

Fig. 1. Topography and bathymetry of the Sunda Arc and surrounding areas. Red rectangle indicates the area of interest of this study. Inset is the Krakatau complex corresponding to red rectangle. Coastal line of Krakatau Island before the catastrophic 1883 eruptions is indicated by black dashed line. Caldera corresponding to the ~530 AD eruption is marked by red dotted line.

attributed to 60,000 BC (Ninkovich, 1979), further indicating the cyclic behavior of the Krakatau eruptions.

Rakata is the part of Krakatau Island which remained after the catastrophic 1883 eruption. Anak Krakatau ("the child of Krakatau") appeared in 1927. Today, Anak Krakatau is a typical cinder cone with an approximate radius of 2 km. It rises up to 315 m above sea level and shows ongoing moderate activity, having grown at an average rate of ~8 cm/week over the last 80 years.

The 1883 eruptive events which began in May, 1883, and concluded on August 27th 1883 with the catastrophic explosion that almost completely destroyed the island and gave rise to a tsunami of 30–40 m in height (e.g. Yokoyama, 1981). It killed more than 36,000 people in the coastal areas of the Indian Ocean. The pyroclastic surge and its deposits on the islands NW of Krakatau and the mainland is discussed extensively in Carey et al. (1996). About 20 km^3 of volcanic material was erupted during the 1883 eruption (e.g., Self and Rampino, 1981; Simkin and Siebert, 1994), and the ash column reached 30 km altitude. The explosions could be heard in a radius of 4000 km, and the air wave reverberated around the earth about seven times (Harkrider, 1967).

The bimodal nature of the Krakatau complex, with extended periods of basaltic and/or basaltic-andesitic eruptions culminating in colossal caldera forming ignimbrite eruptions before the cycle recommences at the basalt stage, was discussed by Van Bemmelen (1949), and has since been strengthened by findings of other authors (Camus et al., 1987; Mandeville et al., 1996a, 1996b).

Currently, Anak Krakatau generally erupt feldspar-rich basaltic andesites with silica contents of ~53–56 wt.% (Dahren, 2010), suggesting that their source is already slightly evolved. This may imply that residual magma from the 1883 eruption may be involved or that rapid differentiation of basaltic magmas from a deeper source has occurred.

The location of the Krakatau volcanic complex in the Sunda Strait is characterized by anomalously strong and frequent volcanic activity, as compared to other parts of the Sunda Arc. This can be explained by a hypothesis that the magmatism in the Krakatau area is not merely caused by subduction processes, but might also be due to extensional tectonism in the Sunda Strait (Nishimura and Harjono, 1992), attributed to the rotation of Sumatra in relation to Java. In Sukadana, ~100 km north of Krakatau along the same volcanic lineament, the influence of the rifting is manifested as an 0.8–1.2 Ma old MORB-type basalt is found (Nishimura and Harjono, 1992). Further research into the depth structures beneath the Krakatau complex may give valuable information for the prognoses of future catastrophic eruptions at Krakatau.

Despite global interest in the activity of Krakatau, a relatively few geophysical and petrological studies were performed in the Krakatau archipelago. Investigations of local seismicity and S-wave attenuation by Harjono et al. (1989) found evidence for multiple levels of magma storage beneath Krakatau, likely located at depths of about 9 and 22 km. The characteristics of the calderas formed by the ~535 AD and 1883 eruptions, as well as of feeding channels, were studied by gravity modeling in Deplus et al. (1995). These authors found a large flat-bottomed 240 m deep depression to the SW of Anak Krakatau, interpreted as a caldera caused by previous eruptions. Seismic tomography has never been applied to Krakatau on a local scale, however.

A multidisciplinary project, KRAKMON, was initiated by researchers from BGR (Germany) in 2005 (Hoffmann-Rothe et al., 2006), including various research approaches such as: measurements of local seismicity (Ibs-von Seht, 2008), electromagnetics, deformation analysis using GPS, ground temperatures, meteorological parameters, sea level, chemical and physical parameters of fumarole gasses, and optical monitoring. Here we consider the seismological data collected from local seismicity to derive a 3-D seismic model beneath the Krakatau complex.

2. Data and algorithm

The seismic network deployed at Krakatau and in surrounding areas is shown in Fig. 2. Within the project 14 seismic onshore stations were installed. The majority of them were located on the central

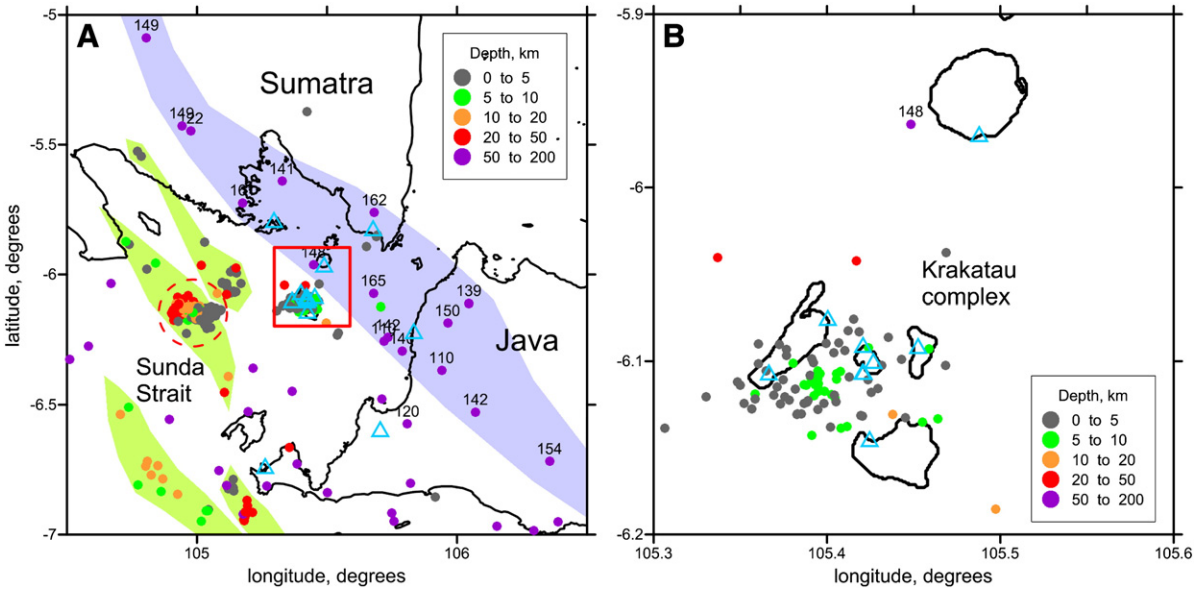

Fig. 2. Configuration of the observation system in the Krakatau area (red rectangle in Fig. 1). A: entire area of interest. B: Krakatau complex corresponding to red rectangle in A. Blue triangles: stations of the seismic network. Dots depict the events registered during the project. Colors reflect the depth of events. For events deeper than 100 km the depth values are indicated. Shaded violet area marks the belt of deep seismicity (>100 km depth). Areas of shallow seismic activity are highlighted in green. Dashed red line indicates a zone of a vertically oriented cluster.

volcano and surrounding islands. Some stations were located on the coasts of Java and Sumatra, and also on remote islands in the Sunda Strait. No ocean bottom stations were used in this project and the network installation was limited to the onshore areas. The network configuration appears to be unfavorable for tomographic research; therefore it is extremely important to assess the reliability of the derived patterns based on a set of different tests provided in this study.

A map of seismic event epicenters registered during the project is shown in Fig. 2. The only criterion for data selection was the total number of P and S onset times per event should not be less than 7. In case of fewer onset times, the location becomes unstable and velocity parameters retrieved from such data are unreliable. Selecting events of more than 7 onset times significantly reduces the dataset volume and introduces more gaps in the ray coverage, reducing the spatial extent of the model. In many tomographic studies events located outside the network (azimuthal gap>180°) are rejected. We did not apply this criterion. As shown by Koulakov (2009a)), out of-network data are extremely important for expanding ray-density and ray-coverage in regions with relatively few earthquakes located within the bounds of the seismic array. Their rejection (if the gap criterion is applied) reduces the datasets and makes the ray coverage less favorable for tomographic inversion.

We admit that the out-of-network events may be located with significant error due to the trade-off between origin time, distance to source and absolute velocities. These factors may lead to bias of absolute times, but the residuals due to seismic patterns in the study area remain weakly affected. As a result, in case of using these data, relative seismic anomalies in the inversion appear to be more stable than the absolute velocities.

In total, we selected 730 events with 3128 P- and 2050 S-phases. This dataset includes some deep focused events with depths of more than 100 km (for such events the depths are indicated in Fig. 2 and highlighted with violet area). Most of these events are located with a small offset to the north-east in respect to the Krakatau complex. These events enable steep ray paths which allow exploring the deep continuation of the volcanic structures. Many shallow events (0–10 km depth) are located beneath the Krakatau complex, which is favorable for retrieving absolute values of Vp, Vs and Vp/Vs ratio in the uppermost sections beneath this part of the study area.

We used the freeware LOTOS code (www.ivan-art.com/science/LOTOS) for the tomographic inversion. Detailed description of this code can be found in manuals on the web site and in Koulakov (2009b). The input data for the code are station coordinates and P- and S-wave arrival times of local earthquakes. The code can start performing calculations without using any a priori information on the sources. In this case, searching for the event locations starts from the center of the network or from the station with minimal travel time. It was shown in previous works (e.g. Koulakov, 2009a, 2009b) that the location algorithm is very stable and it enables the same solution for a source even if the starting positions for the search are located hundreds of kilometers apart.

The calculations based on the LOTOS code include the following steps:

(1) Simultaneous optimization for the best 1-D velocity model and preliminary localization of sources. The location algorithm at this stage is based on a grid-search method and uses tabulated travel times that were previously computed in a 1-D velocity model.
(2) Localization of sources in a 3-D velocity model. At this stage, the ray tracing is performed in a 3-D velocity model using a bending algorithm.
(3) Parameterization (only in the 1st iteration). In this study we use the node parameterization. A set of nodes is distributed in the study volume according to the ray density. The nodes are based on vertical lines distributed regularly in map view (in this study with steps of 3×3 km). In each vertical line, the nodes are installed according to the ray distribution. In the absence of rays, no nodes are installed. The total numbers of nodes were about 500 and 400 for P and S models, respectively. Between the nodes, the velocity distribution is approximated linearly. In order to make the solution grid independent we perform the inversions for several differently oriented grids (e.g. with basic orientations at 0, 22, 45 and 66) and then compute an average model. Examples of node distributions for two grids in horizontal and vertical sections are shown in Fig. 3.
(4) Matrix calculation and inversion. The first derivative matrix is computed along the rays derived after step (2). The matrix also includes the elements responsible for station and source

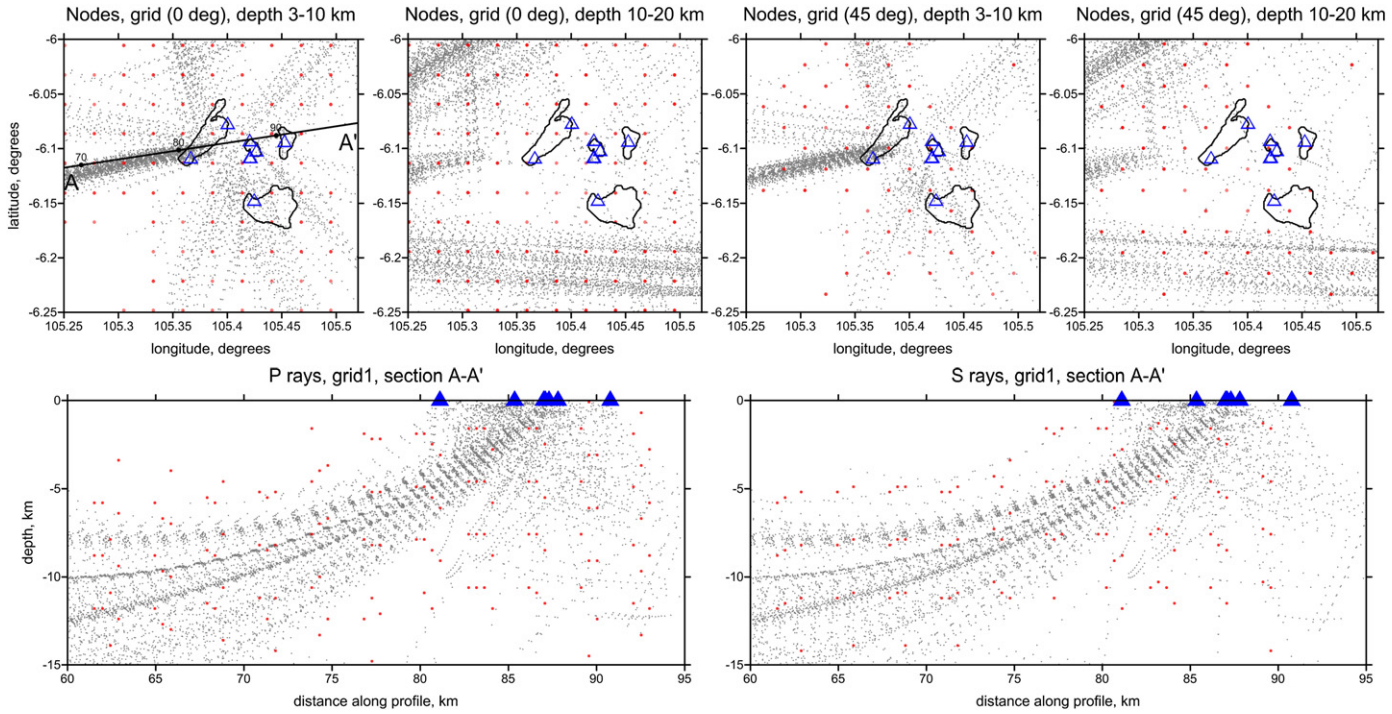

Fig. 3. Examples of node parameterization used for real data inversion. Grids with orientations of 0 and 45 degrees are shown. Red dots are nodes of the grid. Gray dots indicate ray paths in the depth interval 3 to 10 km and 10–20 km, respectively. Blue triangles: stations of the seismic network.

corrections (four elements for each source). The large sparse matrix is inverted using the LSQR method (Paige and Saunders 1982; van der Sluis and van der Vorst 1987). The inversion is damped by adding special regularization matrix blocks for amplitude tuning and smoothing.

(5) After performing the inversion in differently oriented parameterization grids, an average model is computed in a regular grid. This model is used as a basic velocity distribution for the next iteration which comprises steps 2, 4 and 5.

The values of all free parameters (number of iterations, weights, amplitude damping, smoothing, grid spacing, etc.) used for the inversion are estimated based on synthetic modeling.

3. Results and verification

We performed a number of inversions of real data to explore the influence of different parameters and starting models on the results. This is especially important since the considered dataset is based on a rather poor geometric configuration of the network. First of all, we concluded that 1-D optimization at a preliminary step did not provide satisfactory results. After performing a number of trials, we understood that the resulting 1-D models were strongly dependent on starting distributions and selection of parameters. We therefore skipped this automatic optimization step and performed manual tuning of the starting model. We start with a simple 1-D P-velocity model (Table 1) and performed the full tomographic inversion for different values of the Vp/Vs ratio. Comparison of the residual RMS after five iteration steps presented in Table 2 shows that the best result is obtained for Vp/Vs = 1.77. Note that the configuration of the main patterns in different models did not change considerably.

The LOTOS code allows performing the inversion according to two different schemes: for Vp and Vs anomalies (hereafter called as Vp-Vs scheme) using P and S residuals (dt_p and dt_s) and for Vp anomalies and Vp/Vs ratio (Vp-Vp/Vs scheme) using dt_p and differential residuals, dt_s - dt_p. Details of matrix calculation for the cases of Vp–Vs and Vp–Vp/Vs inversions are described in detail in Koulakov et al. (2007). When performing both schemes, we have additional constraints for the damping parameters that should enable similar results in these two cases. The inversion parameters were tuned to achieve maximal similarity of Vs, as well as of Vp/Vs distributions in these two schemes.

In Figs. 4 and 5 we present the results of real data inversion in horizontal and vertical sections. Note that Vp and Vs models are

Table 1
Reference model for P velocity.

Depth (km)	Vp (km/s)
−1	5.02
10	6.90
20	7.70
30	8.00
120	8.05
165	8.17
210	8.30

Table 2
Values of RMS of residuals in 1 and 5 iterations for several starting models with different values of Vp/Vs ratio.

Vp/Vs	RMS of residuals (s) after 1 iteration		RMS of residuals (s) after 5 iteration	
	P-model	S-model	P-model	S-model
1.70	0.2643	0.4214	0.1386	0.1629
1.72	0.2525	0.3790	0.1347	0.1529
1.75	0.2548	0.3490	0.1329	0.1467
1.77	0.2586	0.3465	0.1294	0.1433
1.78	0.2655	0.3463	0.1307	0.1376
1.8	0.2790	0.3535	0.1341	0.1425

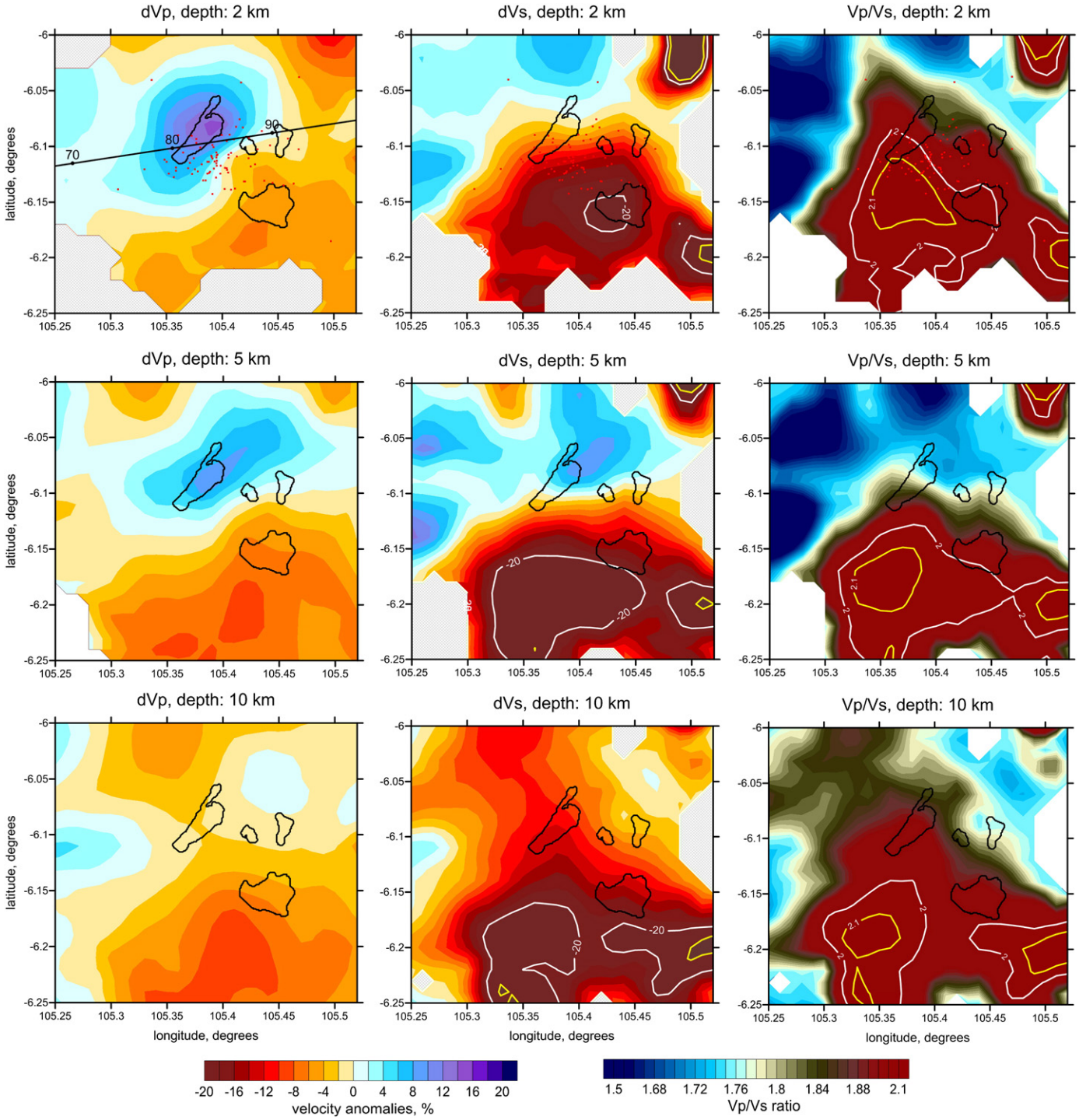

Fig. 4. Distribution of P and S anomalies (calculated using Vp-Vs inversion scheme) and distribution of the Vp/Vs ratio (calculated using Vp-Vp/Vs inversion scheme) in different horizontal sections (at depths of 2 km, 5 km and 10 km). Zones of anomalously high Vp/Vs ratios are indicated by the yellow and white contour lines. Red dots depict the events registered during the project. White and yellow contour lines within high values of Vp/Vs mark the levels of 2 and 2.1. Contour lines in dVs plots indicate levels of 20% (white) and 25% (yellow).

obtained using the Vp-Vs scheme, while Vp/Vs is derived from the Vp-Vp/Vs inversion. Here we show the result only around the Krakatau archipelago down to 13 km depth, whereas, the solution was computed for a much larger area. This selection is made because outside areas are strongly affected by trade-off effect between velocities and source parameters that lead to strong smearing. In this sense, the outside anomalies play the role of source correction and do not probably represent the real velocity distribution. In the selected area, the resolution appears to be reasonable.

Before discussing the main results of real data inversion we will present several tests to check the reliability of the computed models. The LOTOS algorithm allows for definition of various synthetic models, either as periodical anomalies in the checkerboard test or manually by drawing shapes in vertical or horizontal sections. The travel times for the synthetic tests were computed for sources and receivers corresponding to the real observation system. The bending algorithm was used for the 3-D ray tracing in the synthetic model. We added random noise with a magnitude that provided the same

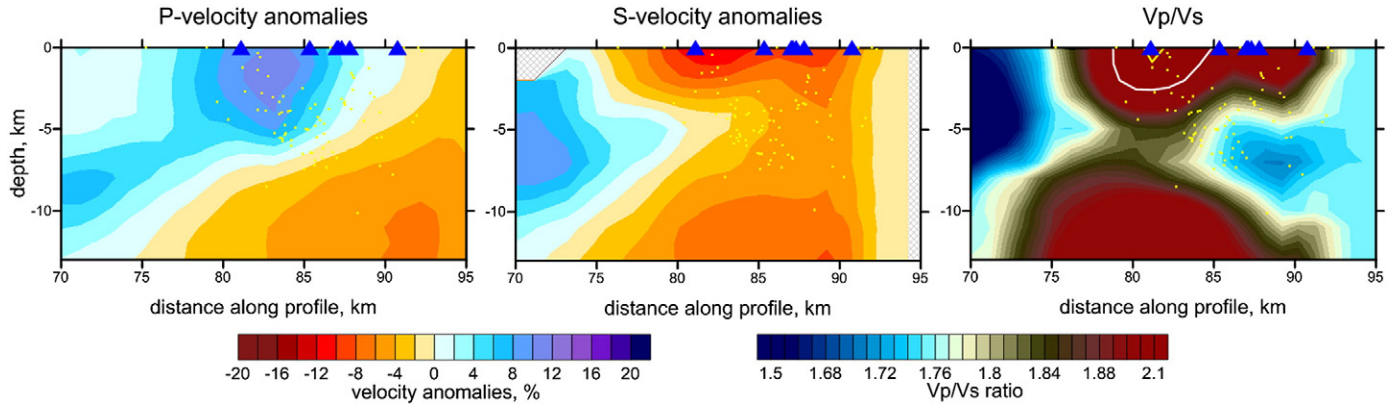

Fig. 5. Vertical sections of the distributions of P and S anomalies (calculated using Vp-Vs inversion scheme) and Vp/Vs ratio (calculated using Vp-Vp/Vs inversion scheme), obtained from real data inversion. Location of the profile is indicated in Fig. 4. Blue triangles: seismic stations. Yellow dots: final locations of the sources. Zones of anomalously high Vp/Vs ratios are indicated by the white contour line.

variance reduction as after the real data inversion. These travel times were the input for the whole inversion procedure, including the step of finding the source locations. The values of the inversion parameters for the synthetic tests were the ones that are used for the real data inversion.

We have performed several tests with different configurations of synthetic anomalies. Here we present one test which adequately represents the real situation (Fig. 6). The synthetic model includes a pair of anomalies located one under another in the area of the Krakatau complex. The lateral size of the upper anomaly is 4×4 km and the lateral size of the lower anomaly is 6x6 km. The upper and lower anomalies are defined in the depth ranges of 0–4 km and 6–10 km, respectively. In these anomalies we defined positive P-anomaly (+6%) and negative S-anomaly (−6%) that resulted at strong positive Vp/Vs ratio. In addition, to assess the effect of smearing due to outside anomalies, we defined a large negative anomaly located to the SW of the Krakatau complex with the amplitude of −6% for P- and S-anomalies. This anomaly strongly affects the travel times of the rays from events located inside. We present the results of the reconstruction in Fig. 6 for P- and S-anomalies and Vp/Vs ratio in one horizontal and one vertical section. The results of this test show that the target anomalies are resolved at correct locations, although they appear to be strongly smeared. It can be seen that P and S anomalies are resolved much less robustly than Vp/Vs patterns. In discussion we will focus mostly on the results of Vp/Vs inversion, whereas the P- and S- anomalies will be interpreted only at a qualitative level. It is important that we do not observe any bias of relevant anomalies in the target area caused by the large outside pattern.

To estimate the effects of random factors and to check the robustness of the obtained anomalies we performed a test with the inversion of independent data subsets. In this test, the entire dataset was randomly subdivided into two similar groups (for example, events with odd and even numbers). Comparison of the inversion results for different subsets with each other, as well as with the

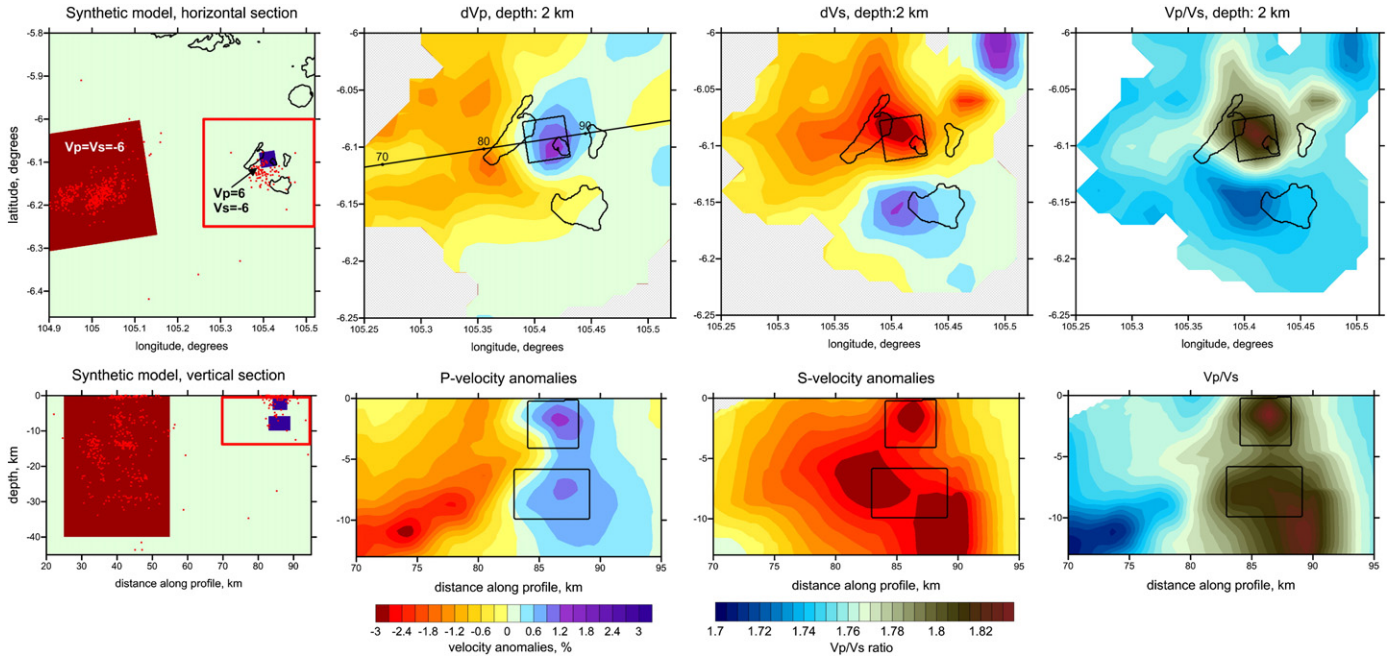

Fig. 6. Synthetic test with realistic anomalies. Left column present the shapes of synthetic anomalies in horizontal (upper) and vertical (lower) sections. Red dots depict the locations of the events. Red rectangle depicts the target area in which the reconstruction results are presented. Columns 2 to 4 show the reconstruction results for P and S-anomalies and for Vp/Vs ratio in horizontal and vertical sections. Contours of synthetic anomalies are depicted by black lines. Location of the vertical section is shown in map with result of dVp reconstruction.

results of the entire data inversion, demonstrates the degree of correlation for both, the P and S models and shows whether the result is robust and unaffected by random factors. Results of this test are presented in Fig. 7. The main features discussed here can be clearly identified in both cases, and thus our model results appear reasonably robust.

4. Discussion and interpretation

4.1. Distribution of seismicity

The seismic events located in the study area (Fig. 2) can be separated into three groups. The first group contains deep focused events with a depth of between 100 and 160 km (purple area in Fig. 2A). These events are lying beneath the volcanic arc and are probably caused by phase transitions in the subducting slab that lead to an active release of fluids into the mantle wedge (e.g. Hacker et al., 2003). Ascent of these fluids leads to decreasing melting temperature above the slab and gives rise to wedge melting diapirs and magma chambers (Poli and Schmidt, 1995). A similar link of seismicity at 100–150 km depth with volcanic arcs is observed in most subduction zones. In some places, the paths of fluids are visible in the results of seismic tomography studies as low-velocity and/or high-attenuation patterns (e.g. Nakajima et al. (2001), for Japan, Haberland and Rietbrock (2001), for Central Andes, Koulakov et al. (2007, 2009a), for Central Java, Koulakov et al. (2009b), for Toba caldera). In most areas these paths appear to be inclined to various angles. Among these examples, only in the area of Toba Caldera, where the strongest Cenozoic eruption occurred 70,000 yr ago, the volcano is located just above the seismicity cluster at 150 km depth, and the low-velocity pattern which links the cluster with the caldera is vertical. The case of Krakatau appears to be similar to that of Toba: the seismicity is shifted laterally to only ~20 km in respect to the volcano complex. We cannot construct the velocity model down to this cluster (100–150 km depth), but in the depth interval where our model is constrained (down to 13 km), we observe a clear vertical low-velocity and high-Vp/Vs pattern which seems to link the volcanic complex with the seismicity cluster. In this sense, Toba and Krakatau volcanoes look similar, which may give a hint for the causes of their exceptional eruption activity.

The second group of events includes tectonic events at shallower depths in the Sunda Strait (green areas in Fig. 2A). In the SW border region of the Sunda Strait, they form linear patterns that correlate with the distributions of the main faults in the study area (Nishimura et al., 1986, Harjono et al., 1991, Pramumijoyo and Sebrier, 1991). An interesting cluster of events is observed at 40 km west of Krakatau (highlighted with red dotted line in Fig. 2A). This cluster forms a vertical, NWW-dipping column. Most of the cluster events occur in a high-velocity area. These events probably represent processes in the lithosphere and maybe rifting related to the opening in the Sunda Strait basin. Note that the deepest events in this cluster occur at a depth of about 30 km that is deeper than the Moho, however, we should be careful about these depth determinations because of poor station coverage.

The third group of events is located just around the Krakatau archipelago. As was shown by Ibs-von Seht et al. (2008) volcano-tectonic earthquakes, long-period earthquakes, and tremor are dominant in this cluster which indicates their volcanic origin. Most

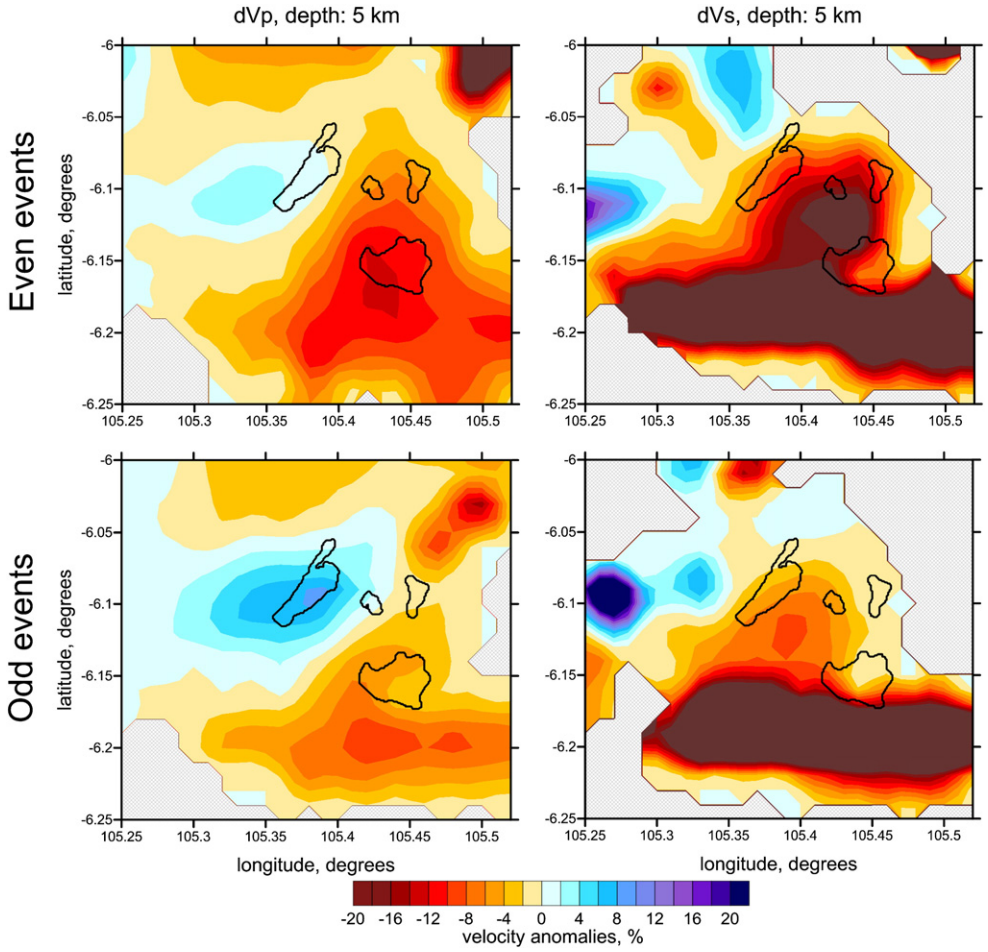

Fig. 7. P and S models obtained as results of inversion of two independent data subsets (odd/even test) presented in one horizontal section (5 km).

of these events occur down to 10 km depth. In vertical sections (Fig. 5), most of them are located in a zone of high P-velocity. In the Vp/Vs plot, the events are mostly concentrated in the transition zone from high to low Vp/Vs ratios. It is interesting to note that most of the seismic activity is located at depths from 2 to 5 km where anticorrelation of P and S velocities is observed and S velocity starts to increase. In regions where both P and S velocities are low, no seismic events below 5 km are observed. The locations of the volcanic events reveal a large volume of material beneath the caldera which is presently active.

4.2. Seismic velocities and Vp/Vs ratio

The resulting P and S anomalies, as well as Vp/Vs ratios are presented in three depth levels (Fig. 4) and one vertical section (Fig. 5). Synthetic tests show that the resolution of the tomographic model is strongly limited. We can only trust the results in the central part of the study area, just beneath the Krakatau complex. In marginal areas the results should be considered with prudence. The anomalies are shown only in areas around parameterization nodes (at a distance less than 5 km from the nearest node) where a sufficient number of rays exist.

The general magnitude of computed P and S anomalies beneath Krakatau is not exceptionally high. For the area beneath the Krakatau complex, the anomalies of P and S velocities do not exceed 8% and 13% respectively. However, very low (20%) and spatially large anomaly of S velocity is observed at south of volcanic complex. For comparison, beneath the Toba Caldera Koulakov et al. (2009b) obtained 16% and 18%. In Central Java, according to Koulakov et al. (2007, 2009a), the amplitudes of P and S anomalies reach 30%. Note that in all these cases, the same tomographic algorithm was used. The most striking feature of this study is an anticorrelation of higher P and lower S velocities just beneath the Krakatau complex down to a depth of 4–5 km. In other parts of the study volume we observe rather good qualitative correlation of P and S anomalies.

Anticorrelation of P and S velocities just underneath the volcano, coupled with clear evidence for magma solidification (crystallization), reflects the presence of a magma chamber system. Indeed, the material in the chamber, brought from depth, has quite different composition and high values of P velocity compared to surrounding rocks. The presence of registered S waves traveling through this anomaly indicates that the magma reservoirs underneath Krakatau are not entirely liquid. One explanation is that the magma chamber consists of partially solidified magma (i.e. low melting percentage), thus not preventing propagation of S waves. Another explanation would be that the reservoirs are not uniform and consists of a set of small pockets of melt in a solid frame. In both cases, substantial decreasing of the S velocities should be observed.

Note that besides the melting and fluid content, the Vp/Vs may also reflect some compositional factors (Christensen, 1996). For example, the abundance of quartz and plagioclase feldspar is the dominant effect in igneous rocks. Mafic plagioclaserich rocks, such as gabbro, have a Vp/Vs ratio of 1.87. Brocher (2005b) also shows that melt is not needed to explain Vp/Vs ratios between 1.81 and 1.87; these values are consistent with solid mafic rocks. However, the observed in this study high Vp/Vs ratios reaching 2.0–2.2 can hardly be due to rock composition. On the contrary, the composition factor may appear to be the most important for the northern half of the target area, where the Vp/Vs ratio is very low (less than 1.5). We propose that this part is composed of hard solidified rocks corresponding to older eruption stages. However we do not have sufficient information to quantify this hypothesis.

The most interesting result of this study is the distribution of Vp/Vs ratios in the vertical section (Fig. 5). Beneath the Krakatau complex we observe a highly heterogeneous structure with two clearly distinguished zones of extremely high Vp/Vs ratio. Note that the starting model, Vp/Vs was constant and equal to 1.77. In the final model, extreme values of 1.45 (west of Krakatau) and 2.2 (beneath Krakatau) are reached. In the vertical section we can see a clear transition between two high-Vp/Vs zones at a depth of about 7 km. This fits with a concept of several levels of chambers/reservoirs beneath Krakatau which also follows from petrological studies discussed below (Fig. 8).

Geobarometric models are calibrated using mineral-melt compositions and are ideally suited for independently testing the results presented above. Mineral chemistry of clinopyroxene and plagioclase in basaltic-andesites erupted from Anak Krakatau in the period 1990–2002 have been analyzed (Dahren, 2010; Dahren et al., 2010) and will be summarized only briefly herein. Two clinopyroxene-melt geobarometeres (Putirka et al., 2003; Putirka, 2008), and a plagioclase-melt geobarometer (Putirka, 2005) were employed. An array of equilibrium tests, as suggested in Putirka (2008), was successfully performed for all mineral-melt pairs used in the study. The clinopyroxene-melt and plagioclase-melt geobarometers resulted in two separated sets of depth estimates with very little overlap in-between. This is indicative of at least two broad, but distinct magma crystallization (storage) regions. The computed depths of plagioclase and clinopyroxene crystallization are focused to in the regions of 4–6 and 8–12 km, respectively.

The depth calculated for plagioclase crystallization (4–6 km) fits well with previously calculated plagioclase crystallization depths (Camus et al., 1987; Mandeville et al., 1996a). The zone of clinopyroxene crystallization (8–12 km) in turn coincide with the findings of the microseismic study in Harjono et al. (1989), identifying a magma chamber system at a depth of ~9 km, however, with an unknown downward extension. The contrasting depth calculations for plagioclase and clinopyroxene crystallization levels are not contradictory. In contrast, plagioclase represents a later stage of magmatic crystallization than clinopyroxene. Hence, the recently erupted magma batches record a mid-crustal magma storage region (dominantly clinopyroxene crystallization) as well as a shallow

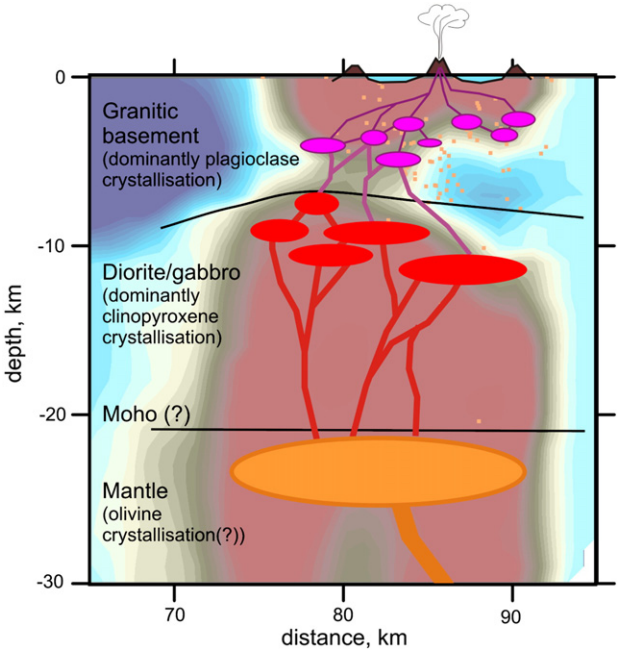

Fig. 8. Interpretation cartoon for the distribution of magma chambers beneath the Krakatau complex. Location of the caldera and the active Anak Krakatau is schematically shown. The background is the distribution of Vp/Vs ratio in the vertical section, same as in Fig. 5. Red dots depict the seismicity around the section.

crustal one (dominantly plagioclase crystallization). The geobarometric study does not reveal evidence for a very deep storage zone that is located below the Moho (>22 km) as suggested by Harjono et al. (1989). This implies that crystalline phases formed in such a deep storage region are unlikely to survive ascent and crustal storage unmodified and the barometry method may be unable to resolve crystallization at greater depth in a complex multi-chamber system.

Geobarometric data, however, provide unequivocal and independent evidence for at least two distinct magma storage regions below Anak Krakatau. One at a depth of approximately 4–6 km and another at 8–12 km. Note that these zones agree remarkably well with lithological crustal boundaries inferred for the bedrock below Anak Krakatau based on evidence from drill holes, xenoliths and microseismic studies (Hamilton, 1979; Oba et al., 1983; Harjono et al., 1989; Harjono et al., 1991; Mandeville et al., 1996b; Kopp et al., 2001; Dahren, 2010; Gardner et al., 2007, J. Petrol.).

5. Conclusions

In this study, we present a first tomographic model with the distribution of P and S velocities and Vp/Vs ratio using local seismicity data. Based on the results, we found indications for a multilayered structure of a magma chamber system beneath the Krakatau complex which seems to be in accordance with petrological studies (mineral-melt equilibria). Although the data distribution was not favorable for a tomographic inversion, we presented a number of tests which reveal the resolution capacity of the tomograms and allow revealing several robust features. This approach should be continued at Anak Krakatau with the deployment of a larger network, preferably to be equipped with ocean bottom seismometers.

Acknowledgments

The KRAKMON project was funded by the German Federal Ministry of Education and Research (BMBF) within the framework of the GEOTECHNOLOGIEN program (FKZ03G0578A). Part of the equipment for the station network was kindly made available by the geophysical instrument pool of the GFZ Potsdam. The work of Ivan Koulakov and Kairly Jaxybulatov is supported by the Helmholtz Society and RFBR Joint Research Project 09-05-91321-SIG a, Multidisciplinary Projects SB RAS #21, and Project ONZ RAS #7.4. Dahren and Troll were supported by the Swedish Science Foundation (VR) through project “Java Segment” to VRT. We also thank the Krakmon field crew, namely Rudolf Knieß, Arne Hoffmann-Rothe, Cahya Patria, Ahmad Solikhin, Michael Lindemann, and Samsul.

References

Brocher, T.M., 2005. Compressional and shear wave velocity versus depth in the San Francisco Bay Area, California: rules for USGS Bay Area Velocity Model 05.0.0. U.S. Geol. Surv. Open-File Rept http://pubs.usgs.gov/of/2005/1317/. 2005–1317, 58 p.

Camus, G., Gourgaud, A., Vincent, P.M., 1987. Petrologic evolution of Krakatau (Indonesia): implications for a future activity. J. Volcanol. Geotherm. Res. 33, 299–316.

Carey, S., Sigurdsson, H., Mandeville, C., Bronto, S., 1996. Pyroclastic flows and surges over water: an example from the 1883 Krakatau eruption. Bull Volc 57, 493–511.

Christensen, N., 1996. Poisson's ratio and crustal seismology. J. Geophys. Res. 101, 3139–3156.

Dahren, B., 2010. Investigating magma plumbing beneath Anak Krakatau volcano, Indonesia: evidence for multiple magma storage regions. Masters Thesis, Uppsala University. ISSN 1650–6553, no: 193.

Dahren, B., Troll, V.R., Andersson, U.B., Chadwick, J.P., Gardner, M.F., 2010. Investigating magma plumbing beneath Anak Krakatau volcano, Indonesia: evidence for multiple magma storage regions. Geophys. Res. Abstr. 12 EGU2010-6934-1.

DeMets, C., Gordon, R., Argus, D., Stein, S., 1990. Current plate motions. Geophys. J. Int. 101, 425–478.

Deplus, C., Bonvalot, S., Dahrin, D., Diament, M., Harjonoc, H., Dubois, J., 1995. Inner structure of the Krakatau volcanic complex (Indonesia) from gravity and bathymetry data. J. Volcanol. Geotherm. Res. 64, 23–52.

Gardner, M.F., Troll, V.R., Hart, G., Gamble, J.A., Ellam, R.M., Wolff, J.A., Gertisser, R., 2007. Shallow-level processes at Krakatau volcano: crystallization and late stage crustal contamination. Geophysical Research Abstract, EGU meeting Vienna, Austria, EGU07-A-08469.

Haberland, C., Rietbrock, A., 2001. Attenuation tomography in the western Central Andes: a detailed insight into the structure of a magmatic arc. J. Geophys. Res. 106, 11151–11167.

Hacker, B.R., Peacock, S.M., Abers, G.A., Holloway, S.D., 2003. Subduction Factory 2. Are intermediate-depth earthquakes in subducting slabs linked to metamorphic dehydration reactions? J. Geophys. Res. 108. doi:10.1029/2001JB001129.

Hamilton, W.B., 1979. Tectonics of the Indonesian Region. United States Geological Survey Professional Paper, 1078.

Harjono, H., Diament, M., Nouaili, L., Dubois, J., 1989. Detection of magma bodies beneath Krakatau volcano (Indonesia) from anomalous shear waves. J. Volcanol. Geotherm. Res. 39, 335–348.

Harjono, H., Diament, M., Dubois, J., Larue, M., 1991. Seismicity of the Sunda Strait: evidence for crustal extension and volcanological implications. Tectonics 10, 17–30.

Harkrider, D., 1967. The Krakatoa air-sea waves: an example of pulse propagation in coupled systems. Geophys. J. R. Astron. Soc. doi:10.1111/j.1365-246X.1967.tb02150.x, Issue 1-3, pages 149-159.

Hilton, D.R., Craig, H., 1989. A helium isotope transect along the Indonesian archipelago. Nature 342, 906–908.

Hoffmann-Rothe, A., Ibs-von Seht, M., Knieß, R., Faber, E., Klinge, K., Reichert, C., Purbawinata, M.A., Patria, C., 2006. Monitoring Anak Krakatau Volcano in Indonesia.

Ibs-von Seht, M., 2008. Detection and identification of seismic signals recorded at Krakatau volcano (Indonesia) using artificial neural networks. J. Volcanol. Geotherm. Res. 176, 448–456. doi:10.1016/j.jvolgeores.2008.04.015.

Jarrard, R.D., 1986. Relation among subduction parameters. Rev. Geophys. 24, 217–284.

Judd, J.W., 1889. The earlier eruptions of Krakatau. Nature 40, 365–366.

Kopp, H., Flueh, E.R., Klaeschen, D., Bialas, J., Reichert, C., 2001. Crustal structure of the central Sunda margin at the onset of oblique subduction. Geophys. J. Int. 147, 449–474.

Koulakov, I., 2009a. Out-of-network events can be of great importance for improving results of local earthquake tomography. Bull. Seismol. Soc. Am. 99 (4), 2556–2563. doi:10.1785/0120080365.

Koulakov, I., 2009b. Code LOTOS-10 for 3D tomographic Inversion Based on Passive Seismic Data from Local and Regional Events.

Koulakov, I., Bohm, M., Asch, G., Lühr, B.-G., Manzanares, A., Brotopuspito, K.S., Fauzi, Pak, Purbawinata, M.A., Puspito, N.T., Ratdomopurbo, A., Kopp, H., Rabbel, W., Shevkunova, E., 2007. P and S velocity structure of the crust and the upper mantle beneath central Java from local tomography inversion. J. Geophys. Res. 112, B08310. doi:10.1029/2006JB004712.

Koulakov, I., Jakovlev, A., Luehr, B.G., 2009a. Anisotropic structure beneath central Java from local earthquake tomography. Geochem. Geophys. Geosyst. 10, Q02011. doi:10.1029/2008GC002109.

Koulakov, I., Yudistira, T., Luehr, B.-G., Wandono, 2009b. P, S velocity and VP/VS ratio beneath the Toba caldera complex (Northern Sumatra) from local earthquake tomography. Geophys. J. Int. 177, 1121–1139. doi:10.1111/j.1365-246X.2009.04114.x.

Mandeville, C.W., Carey, S., Sigurdsson, H., 1996a. Magma mixing, fractional crystallization and volatile degassing during the 1883 eruption of Krakatau volcano, Indonesia. J. Volcanol. Geotherm. Res. 74, 243–274.

Mandeville, C.W., Carey, S., Sigurdsson, H., 1996b. Sedimentology of the Krakatau 1883 submarine pyroclastic deposits. Bull. Volcanol. 96, 512–529.

Müller, R.D., Roest, W.R., Royer, J.-Y., Gahagan, L.M., Sclater, J.G., 1997. Digital isochrons of the world's ocean floor. J. Geophys. Res. 102, 3211–3214.

Nakajima, J., Matsuzawa, T., Hasegawa, A., Zhao, D., 2001. Three-dimensional structure of Vp, Vs, and Vp/Vs beneath northeastern Japan: implications for arc magmatism and fluids. J. Geophys. Res. 106, 843–857.

Ninkovich, D., 1979. Distribution, age and chemical composition of tephra-layers in deep-sea sediments off Western Indonesia. J. Volcanol. Geotherm. Res. 5, 67–86.

Nishimura, S., Harjono, H., 1992. The Krakatau Islands: the geotectonic setting. GeoJournal 28, p87–p98.

Nishimura, S., Nishida, J., Yokoyama, T., Hehuwat, F., 1986. Neo-tectonics of the Strait of Sunda, Indonesia. J. Southeast Asian Earth Sci. 1, 81–91.

Oba, N., Tomita, K., Yamamoto, M., Istidjab, M., Badruddin, M., Parlin, M., Sadjiman, Djuwandi, A., Sudradjat, A., Suhanda, T., 1983. Geochemical study of lava flows, ejecta and pyroclastic flows from the Krakatau group, Indonesia: Rept. Fac. Sci. Kagoshima Univ., 16, pp. 21–41.

Paige, C.C., Saunders, M.A., 1982. LSQR: an algorithm for sparse linear equations and sparse least squares. ACM trans. Math. Soft. 8, 43–71.

Poli, S., Schmidt, M.W., 1995. H2O transport and release in subduction zones: experimental constrains on basaltic and andesitic systems. J. Geophys. Res. 100, 22299–22314.

Pramumijoyo, S., Sebrier, M., 1991. Neogene and Quaternary fault kinematics around the Sunda Strait area, Indonesia. J. Southeast Asian Earth Sci. 6 (2), 137–145.

Putirka, K.D., 2005. Igneous thermometers and barometers based on plagioclase + liquid equilibria: test of some existing models and new calibrations. Am. Mineral. 90, 336–346.

Putirka, K.D., 2008. Thermometers and barometers for volcanic systems. In: Putirka, K.D., Tepley, F.E. (Eds.), Reviews in Mineralogy and Geochemistry, 69, pp. 61–120.

Putirka, K.D., Mikaelian, H., Ryerson, F., Shaw, H., 2003. New clinopyroxene-liquid thermobarometers for mafic, evolved, and volatile-bearing lava compositions, with applications to lavas from Tibet and the Snake River Plain, Idaho. Am. Mineral. 88, 1542–1554.

Self, S., Rampino, M.R., 1981. The 1883 eruption of Krakatau. Nature 294, 699–704.

Simkin, T., Siebert, L., 1994. Volcanoes of the World, Geoscience Press in association with the Smithsonian Institution Global Volcanism Program, Tucson AZ, 2nd edition. 368 p.

van Bemmelen, R.W., 1949. The Geology of Indonesia. Martinus Nijhoff, The Hague.

Van der Sluis, A., van der Vorst, H.A., 1987. Numerical solution of large, sparse linear algebraic systems arising from tomographic problems. In: Nolet, G. (Ed.), Seismic Tomography. Reidel, Dortrecht, the Netherlands, pp. 49–83.

Wohletz, K.H., 2000. Were the Dark Ages triggered by volcano-related climate changes in 6th century? Eos 48, F1305.

Yokoyama, A., 1981. Geophysical interpretation of the 1883 Krakatau eruption. J. Volcanol. Geotherm. Res. 9, 359–378.